Electronic Supplementary Material (ESI) for New Journal of Chemistry.

Supplementary Information

Unlocking Potential of MOF-Derived $CaMoO_4$ Electrode for High Performance Supercapacitor Application

Palanisamy Rajkumar[a], Joel Kingston Ramesh[b], Vediyappan Thirumal[a], Maalavika S Iyer[c], Margrate Bhackiyavathi Princess[d], RM. Gnanamuthu[e], Kisoo Yoo[a,*], Jinho Kim[a,*]

[a] Department of Mechanical Engineering, Yeungnam University, Gyeongsan-si, Gyeongbuk-do 38541, Republic of Korea.

[b] Department of Chemistry, Indian Institute of Technology Madras, Chennai 600036, Tamil Nadu, India.

[c] SSN Research Centre, Sri Sivasubramaniya Nadar College of Engineering, Kalavakkam, Chennai 603110, Tamil Nadu, India.

[d] Department of Chemistry, Lady Doak College, Tallakulam, Madurai - 625002, Tamil Nadu, India.

[e]Centre for Nonlinear System, Chennai Institute of Technology, Chennai, 600 069, Tamil Nadu, India.

*E-mail: jinho@ynu.ac.kr (JK); kisooyoo@yu.ac.kr (KY)

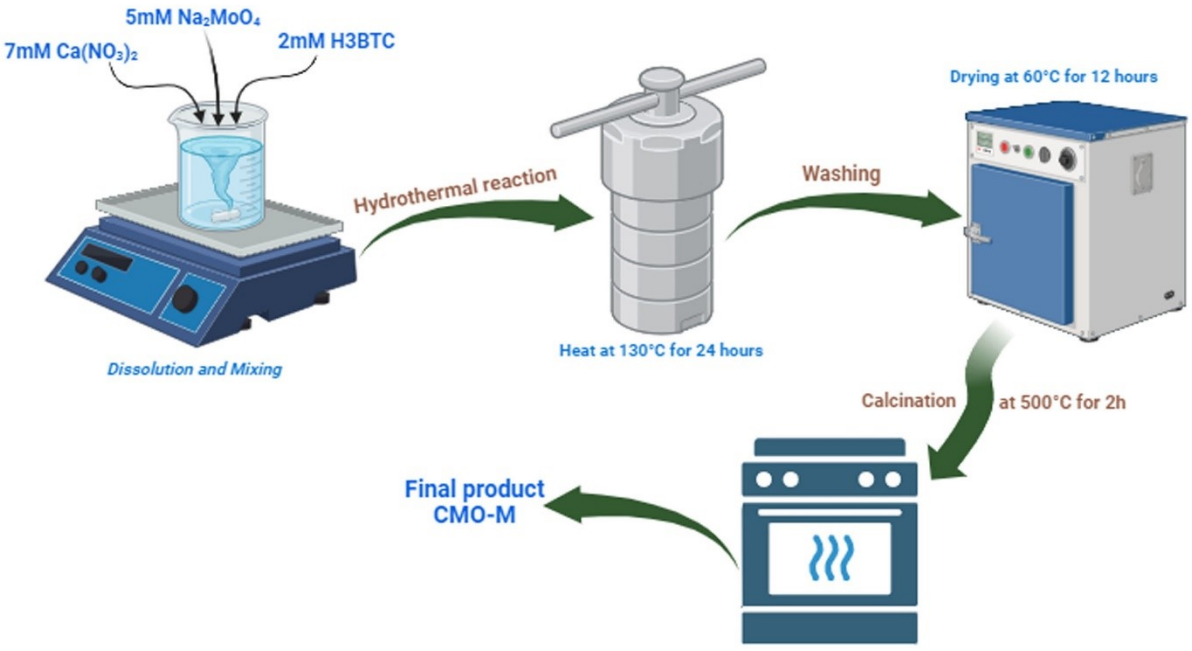

Fig S1: Schematic representation of methodology

Material Characterization:

Powder X-ray diffraction (XRD) patterns were obtained using Cu Kα radiation (λ=0.15418 nm) with an operating condition of 40 mA and 40 kV, covering the range from 5° to 80°, utilizing a Bruck XRD D8 instrument from Germany. Fourier Transform Infrared (FTIR) spectroscopy was employed to analyze the vibration of functional groups, conducted with a Thermo Nicolet 380 spectrometer. The morphologies and elemental compositions of the samples were characterized using scanning electron microscopy (SEM) coupled with energy dispersive spectrometry (EDS) on an S-4800 instrument, as well as transmission electron microscopy (TEM) on a FEI Tecnai 20 G2. Furthermore, the specific surface areas and pore sizes of the precursor were determined through adsorption isotherm analysis using the Brunauer-Emmet-Teller (BET) model, utilizing a Micromeritics ASAP 2010 instrument.

Physical Characterisations

X-Ray Diffraction:

Figure S2 illustrates the X-ray diffraction (XRD) patterns of both pure $CaMoO_4$ (CMO-P) and $CaMoO_4$ samples derived (CMO-M) from Metal-Organic Frameworks (MOFs). Notably, both samples exhibit similar XRD patterns, aligning perfectly with the tetragonal structure of calcium molybdenum oxide (space group I41/a), with lattice parameters a = b = 5.226 Å and c = 11.430 Å, corroborating with the JCPDS card no. 29−0351. The observed XRD peaks at 18°, 28.7°, 31°, 34°, 37°, 47°, 49°, 54°, 58°, and 76° correspond to diffraction from crystal planes (101), (112), (004), (200), (202), (204), (220), (116), (312) and (316), respectively, confirming the powellite structure of $CaMoO_4$ within the scheelite group of the molybdate family. These findings provide crucial insights into the structural characteristics of $CaMoO_4$ samples, laying the foundation for further exploration and optimization in supercapacitor applications [S1, S2]. Moreover, our acquired $CaMoO_4$ samples demonstrate exceptional crystallinity, as evidenced by the minimal peak broadening

observed in the X-ray diffraction (XRD) pattern. This indicates a high level of crystalline perfection, a notable departure from MOF-derived oxides, which frequently display broader diffraction peaks due to framework damage during synthesis. It is noteworthy, however, that faint peaks corresponding to Ca/Mo-MOF structures are still discernible, suggesting incomplete conversion into their respective metal oxides likely due to the optimized calcination temperature required to preserve the MOF structure. It is crucial to emphasize that surpassing a calcination temperature of 500°C may result in structural damage within the framework, as frequently reported in the literature [S3, S4].

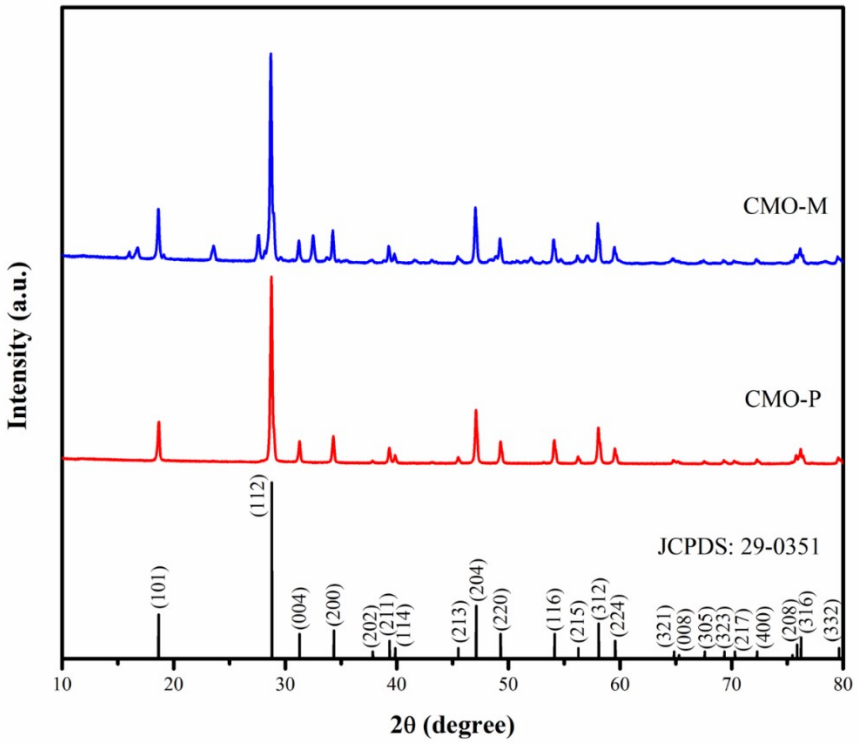

Fig S2: XRD Pattern of CMO-P and CMO-M samples.

Brunauer-Emmett-Teller Method and Pore size distribution:

Both samples displayed Type-IV adsorption isotherms, with CMO-M showing a more extended adsorbate compared to CMO-P, suggesting enhanced porosity. Quantitatively, CMO-P had a specific surface area of 72.34 $m^2 g^{-1}$, while CMO-M exhibited a higher surface area of 104.76 $m^2 g^{-1}$, with corresponding desorption pore sizes of 6.75 nm and 6.345 nm,

respectively. Despite similar pore sizes, a closer examination of the pore size distribution plots revealed a more defined distribution in the mesopore region for CMO-M. This refinement was attributed to a controlled preservation of pore structure during calcination, preventing collapse and resulting in a well-defined pore size distribution. The increase in surface area in CMO-M can also be attributed to the presence of the stabilizing linker, which hindered particle agglomeration.

Scanning Electron Microscopy and Transmission Electron Microscopy:

Figures 2(a) and (b) depict the morphological FE-SEM images of CMO-P and Figure 2(c) and (d) shows the morphology of CMO-M after calcination. From the low-magnification images in Figures 2(a) and (c), both CMO samples exhibit a nanoparticle morphology. The primary disparity between the two samples lies in the smaller particle size and the presence of broken particles observed in the MOF-derived CMO, in contrast to the CMO obtained through conventional hydrothermal synthesis. The broken particle morphology in the MOF-derived $CaMoO_4$ sample is attributed to the intricate nature of MOFs and their transformation during calcination. MOFs, characterized by their porous crystalline structure composed of metal nodes and organic linkers, undergo non-uniform thermal decomposition during the removal of organic components. This process can lead to pore collapse and structural rearrangements within the material. The inherent instability of some MOFs during thermal treatments can break coordination bonds, resulting in the observed fragmented particle morphology. The elemental mapping of the prepared samples confirms the presence of Ca, Mo and O as shown in Figure S3, which also affirms the homogeneous distribution of all the elements. Figure 2(e, f) illustrates the transmission electron microscopy (TEM) image of CMO-M. The image depicts spherical sheet-like structures with evident overlap, suggesting the characteristic morphology of the sample. Notably, the presence of clear boundaries within

the structures serves as evidence of the material's crystalline nature. Upon analysis, the diameter of the CMO-M nanoparticles is calculated to be 250 nm.

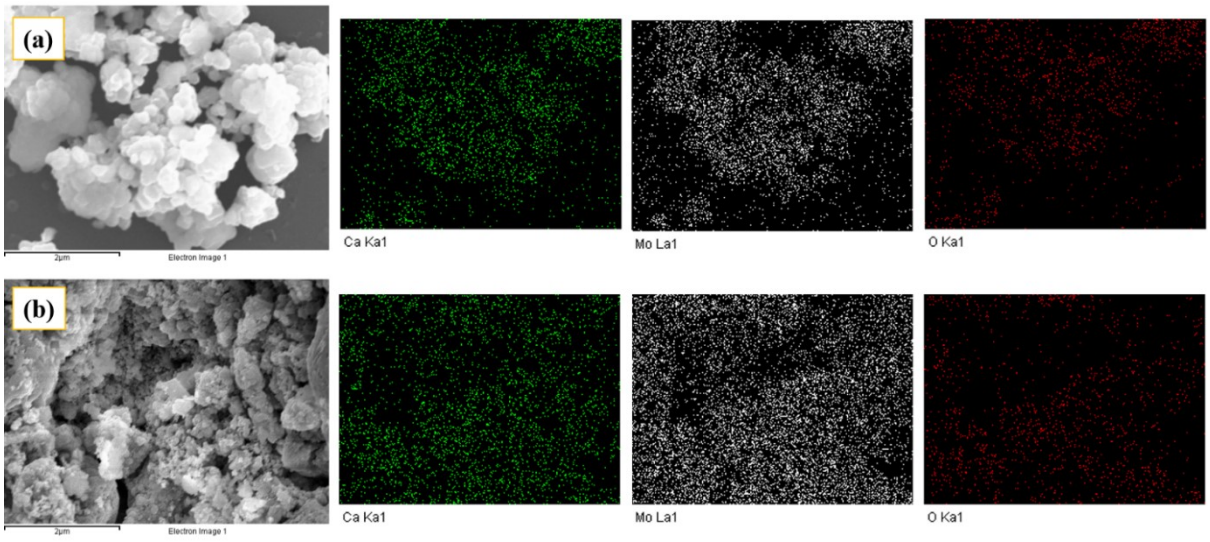

Fig S3: SEM mapping of (a) CMO-P and (b) CMO-M sample respectively

Electrochemical Characterisation:

The pure CMO and MOF-derived CMO were utilized as coatings on Ni foam, serving as the working electrodes for assessing their charge storage capabilities. This evaluation was carried out using a conventional three-electrode configuration in a 3 M KOH electrolyte, with an Ag/AgCl reference electrode and platinum as the counter electrode. CV curves were recorded for both electrodes across different scan rates (10, 20, 40, 60, 80, and 100 mV s^{-1}) within the potential range of 0.0 to 0.55 V (Fig. 3(a, b)).

Specific capacitance in three electrode system:

When the $CaMoO_4$ electrode is introduced into the alkaline electrolyte (KOH) with a pH exceeding 8.0, it is oxidized to form $Ca(OH)_3$ prior to any electrochemical measurements. It has been reported that MoO_2 in the pH range of 8 will not exhibit any redox peaks [S5]. Hence, equation (1) represents the potential redox reaction for both the oxidation and

reduction peaks in the CV curve. As the scan rate increases, there is a noticeable blue shift in the oxidation peak, indicating that the electrochemical process is diffusion controlled.

$$3[Ca(OH)_3]^- \leftrightarrow Ca_3O_4 + 4H_2O + OH^- + 2e^- \quad \text{------(1)}$$

Equation (2) is used to derive the specific capacitance for the prepared samples.

$$C_s = \frac{I.\Delta t}{m.\Delta V} \quad \text{------(2)}$$

Where C_s is the specific capacitance (F g^{-1}), I is the discharge current (A), Δt is the discharge time (s), ΔV is the voltage interval (V), and *m* represent the mass of electroactive material (g). A noticeable inverse relationship between current density and C_s values was noted, indicating limited ionic kinetics during the discharging process. Lower current densities promoted enhanced electrolyte ion penetration through the electrode material, potentially improving the insertion/extraction process and resulting in higher specific capacitance.

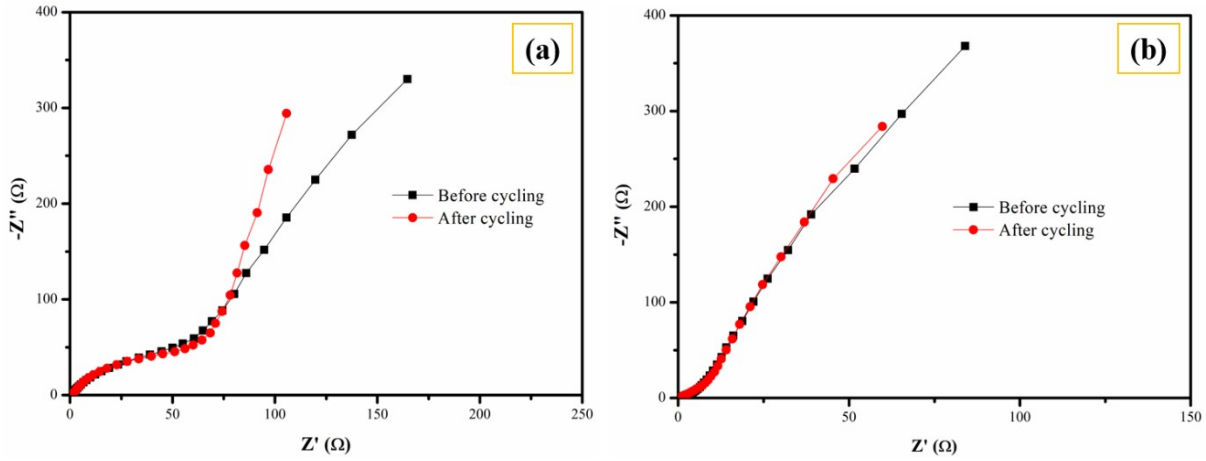

Fig S4: Before and after cycling EIS spectra of (a) CMO-P and (b) CMO-M electrode

In Fig S4, the Nyquist plots reveal distinct features: a semicircular section in the high-frequency range and a sloped line in the low-frequency range. The high-frequency region

depicts the formation of solution resistance (R_s) at the interface between the electrode and electrolyte, while the low-frequency region indicates the induction of electron transfer resistance on the electrode surface. The diameter of the semicircle is directly correlated with the resistance encountered by electron flow at the electrode/electrolyte interface. Specifically, the solution resistance (R_s) for the CMO-P electrode exceeds that of the CMO-M electrode. A smaller solution resistance corresponds to an ideal capacitor behavior with lower internal resistance. Notably, the electron-charge transfer resistance (R_{ct}) for the CMO-M electrode is significantly lower than that of the CMO-P (~65 **Ω**) electrode due to the insulator-to-metal transition of CMO-M at higher concentration of oxygen vacancies. Lower values of solution and charge transfer resistance signify high conductivity of the electrode material, ultimately enhancing the overall performance of the electrode material.

Modified Power's Law – Diffusion and Capacitive controlled process:

The determination of corresponding diffusion and capacitive-controlled reactions occurring at the electrode/electrolyte interface at different scan rates can be achieved using a modified power law, as follows:

$$i_p = k_1 v + k_2 v^{1/2} \quad \text{------(3)}$$

and

$$i_p/v^{1/2} = k_1 v^{1/2} + k_2 \quad \text{------(4)}$$

The total sum of the equation gives the diffusion-controlled process ($k_2 v^{1/2}$) and capacitive-controlled ($k_1 v$) with that of the peak current (i_p). Figure S5(a, b) depicts the slope and intercept value obtained by linear fitting of $i_p/v^{1/2}$ and $v^{1/2}$ values. The slope and intercept values obtained were utilized to ascertain the percentage of diffusion and capacitive contribution. At a scan rate of 10 mV/s, the diffusion-controlled process accounted for 87.8% and 86.06% of the anodic and cathodic peak currents, respectively for CMO-P. For CMO-M,

the diffusion-controlled process accounted for anodic peak is 96.46% and 96.55% for cathodic peak current. On increasing the scan rate (20 to 100 mV s^{-1}) for CMO-P electrode, a decrease in diffusive process (83.6% and 81.36% to 69.5% and 66.1%) and an increase in capacitive process (16.3% to 30.4% and 18.6% to 33.86%) can be observed. For CMO-M electrode, a similar pattern of decrement in diffusive process (95.07% to 89.6% and 95.1% to 89.8%) and an increase in capacitive behavior (4.9% to 10.3% and 4.8% to 10.1%) can be observed. The concurrent increase and decrease of diffusion and capacitive-controlled processes during both anodic and cathodic processes suggest the occurrence of primary ion exchange processes within the electrode. Additionally, the CMO-M electrode was found to exhibit a higher percentage of diffusion-controlled behavior than capacitive-controlled, indicating its battery-type characteristics.

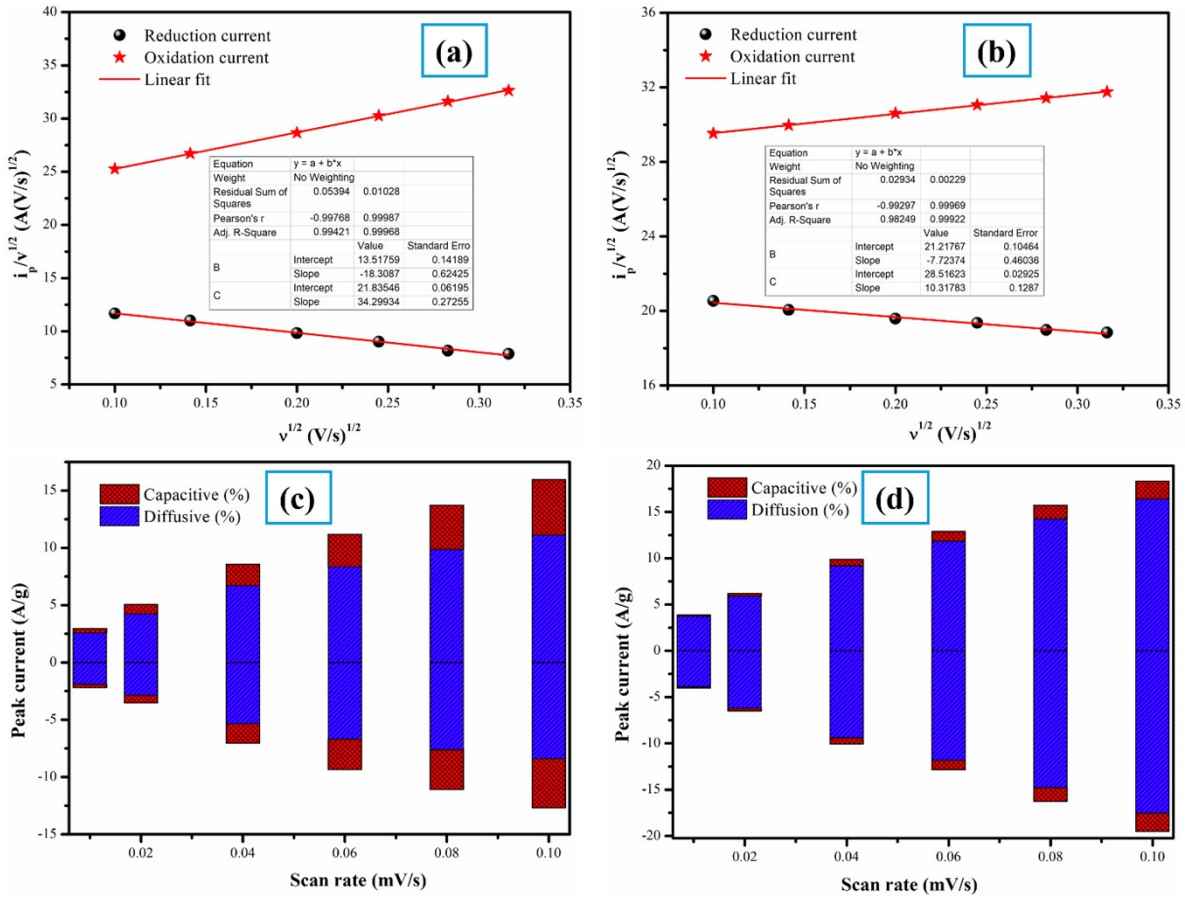

Fig S5: Plot between $i_p/v^{1/2}$ and $v^{1/2}$ of (a) CMO-P and (b) CMO-M and Diffusion controlled and capacitive controlled percentage with peak current of (c) CMO-P and (d) CMO-M device.

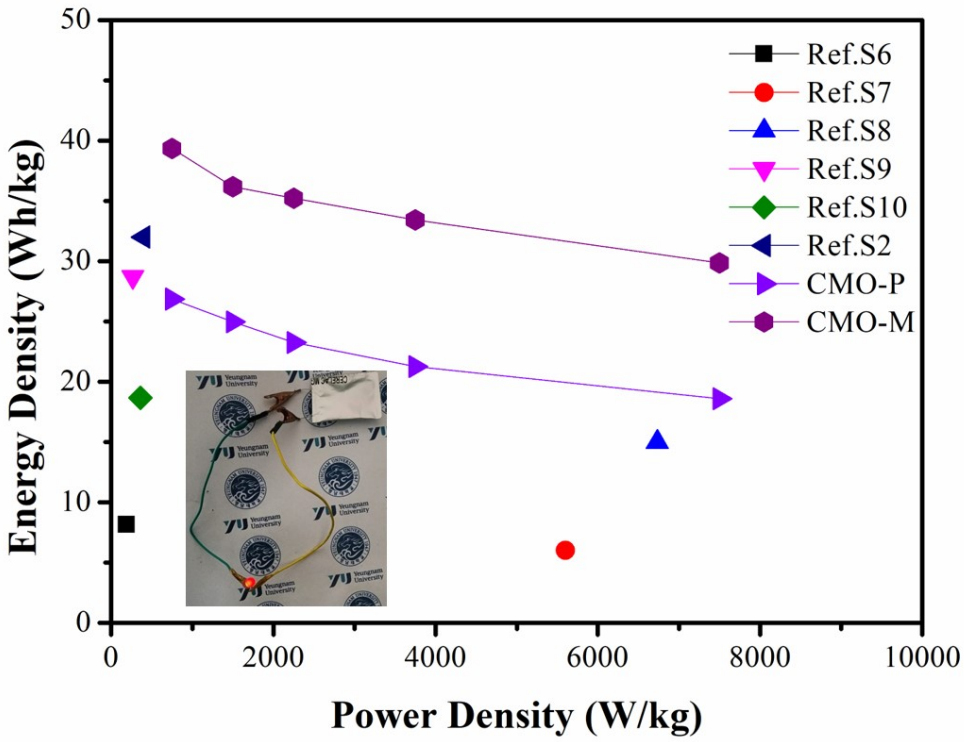

Fig S6: Ragone plot of CMO-P and CMO-M device, (inset: Glowing light bulb powered by the fabricated supercapacitor)

Table S1: Comparison of MOF-derived $CaMoO_4$ device electrochemical performance with previously reported results

Positive electrode	**Negative electrode**	**Specific capacitance (F/g)**	**Energy density (Wh kg^{-1})**	**Power density (W kg^{-1})**	**Cs retention**	**Ref.**
$CoMoO_4$	rGO	26.16 at 1 A g^{-1}	8.17	187.5	84.7% after 4000 cycles	[S6]
$ZnMoO_4$	AC	63.13 at 1 A g^{-1}	6.01	5600.19	-	[S7]
$NiCo_2O_4$@ $MnMoO_4$	AC	-	15	6734	96% after 10,000 cycles	[S8]
$CoMoO_4$@ $NiMoO_4$	AC	-	28.7	267	99% after 3000 cycles	[S9]

$CaMoO_4$	AC	24.16 mAh	18.68	362	85% after 5000 cycles	[S10]
$CaMoO_4$	$CaMoO_4$	72 at 0.25 A g^{-1}	32	400	-	[S2]
MOF-derived $CaMoO_4$	AC	128 at 1 A g^{-1}	39.35	750	88% after 10000 cycles	This work

References:

S1. M. Minakshi, D.R. Mitchell, C. Baur, J. Chable, A.J. Barlow, M. Fichtner, A. Banerjee, S. Chakraborty, R. Ahuja, Nanoscale Adv., 2019, 1(2), 565-580.

S2. M.M. Sundaram, D. Appadoo, Dalton Trans., 2020, 49(33), 11743-11755.

S3. Y. Song, X. Li, L. Sun, L. Wang, RSC Adv., 2015, 5(10), 7267-7279.

S4. A.A. Bhoite, K.V. Patil, R.S. Redekar, J.H. Jang, V.A. Sawant, N.L. Tarwal, J. Energy Storage, 2023, 72, 108557.

S5. M. Minakshi, D.R. Mitchell, C. Baur, J. Chable, A.J. Barlow, M. Fichtner, A. Banerjee, S. Chakraborty, R. Ahuja, , Nanoscale Adv., 2019, 1(2), 565-580.

S6. G.K. Veerasubramani, K. Krishnamoorthy, S.J. Kim, RSC Adv., 2015, 5(21), 16319-16327.

S7. Y.P. Gao, K.J. Huang, C.X. Zhang, S.S. Song, X. Wu, J. Alloys Compd., 2018, 731, 1151-1158.

S8. Y. Yuan, W. Wang, J. Yang, H. Tang, Z. Ye, Y. Zeng, J. Lu, Langmuir, 2017, 33(40), 10446-10454.

S9. Z. Zhang, H. Zhang, X. Zhang, D. Yu, Y. Ji, Q. Sun, Y. Wang, X. Liu, J. Mater. Chem. A, 2016, 4(47), 18578-18584.

S10. J. Bhagwan, S.K. Hussain, J.S. Yu, ACS Sustain. Chem. Eng., 2019, 7(14), 12340-12350.